The Planetary Science Journal, 7:105 (16pp), 2026 May https://doi.org/10.3847/PSJ/ae5b80

Sliding Terrains and Dislocated Plates in Amazonis Planitia (Mars) as the Result of Instability of a Frozen Martian Ocean

Fabio Vittorio De Blasio
Department of Earth and Environmental Sciences—DISAT, University of Milano-Bicocca, Piazza della Scienza 4, 20126 Milan, Italy
Received 2025 December 16; revised 2026 March 6; accepted 2026 March 25; published 2026 May 11

Abstract

Some peculiar landforms over a large area (about 400,000 km^2) of Amazonis Planitia on subequatorial Mars include groups of parallel erosion marks ("grooves") that are some kilometers long and 2 km wide, bright on darker terrain, and associated with light areas interpreted as open fractures hundreds of kilometers wide ("sliding terrain"), mounds located at one end of the grooves, sinuous folds in the rugged terrain, and kilometer-wide blocks that have been roto-translated from their initial position. Similar features in other Martian areas (in particular Athabasca–Cerberus) have been earlier attributed either to volcanic action or to displacement of ice plates. Here the combined analysis of the landforms with mathematical estimates is consistent with the model of floating ice extending over the northern part of Amazonis Planitia. An initial phase, with ice floating on water (likely an ocean), was followed by a drop in water level. As the ice floes came into contact with the gently sloping floor, they no longer floated on an equipotential surface. Tension increased and ice repeatedly broke into smaller pieces that moved for some kilometers, pushed by the weak gradients. The large, bright areas are the product of such fractures. Grooves were formed by ice sliding on the ground, and collisions between floes produced pressure ridges. The depth of the grooves and of sliding terrain, on the order of a few meters, indicates the thickness of the ice sheet, comparable to that of the present-day Arctic. Dating of the ice sliding events and other features are found to be incompatible with volcanic processes.

Unified Astronomy Thesaurus concepts: Planetary surfaces (2113)

1. Introduction

Some landforms south of Elysium Mons on low-latitude Mars (Athabasca Valles–Cerberus Palus) feature enigmatic arrays of several-kilometer-long rigid plates resulting from surface rupture and displacement of a previously intact shield (J. B. Murray et al. 2005). Obstacles protruding from the terrain have scraped away material as plates moved, depositing mounds on the one side, and kilometer-wide wrinkled ridges are visible in the surrounding areas. The major interest with these terrains is their possible icy nature, particularly given the resemblance to plates with giant ice floes floating on the surface of water (J. B. Murray et al. 2005). This observation has important implications, since it requires large amounts of standing water, a key problem in the study of early Mars and astrobiology (e.g., M. H. Carr 1996).

Figure 1(a) identifies the area (here, for simplicity, referred to as the "Athabasca–Cerberus" area), while Figure 1(c) shows an example of platy terrains and related landforms in this area. Note the displaced plates, mounds piled on one side of craters (in the studied examples they are all oriented in the same direction), and wrinkled ridges. Brackenbridge (1993) and Rice et al. (2002), based on Viking and Mars Orbiter Camera images, were the first to note the similarity of these plates to the surfaces of frozen lakes. In line with the work of J. B. Murray et al. (2005), who compared the plates to floating ice in the marine polar region of Earth, M. R. Balme et al. (2010) described the paleogeography of the area in detail, considering these landforms to be the result of ponding water from a young outflow channel pouring into the heavily vulcanized area of Elysium Planitia. However, more recent studies of platy terrains and other distinctive landforms in the Athabasca–Cerberus area have reached radically different conclusions about their nature. J. R. Voigt & C. W. Hamilton (2018) studied platy terrains in southern Elysium, including lobate forms, knobby terrains, and sinuous ridges, distinguishing a total of 19 distinct facies. While admitting that recent flooding explained the presence of a northeast-trending channel and the streamlined islands within it, they nevertheless attributed most of the distinctive terrains to earlier volcanic processes. The terrains were therefore interpreted as the result of a lava crust disintegrating over a basaltic lava flow, and therefore not related to ice.

There is no doubt that volcanic features have profoundly influenced these areas (e.g., J. B. Plescia 1990, 2003). The central question is whether ice was also involved, or whether most or all of the features should be interpreted as volcanic. In many cases, lava flows in the Cerberus Fossae–Athabasca Valleys may represent the product of volcanism on glaciated terrain (W. K. Hartmann & D. C. Berman 2000; W. L. Jaeger et al. 2007). Although areas with similar features are found in other areas of Mars, such as the Kasei–Echus Valleys (R. M. Williams & M. C. Malin 2004; D. W. Leverington 2018), the nature of these plates and associated landforms (icy versus volcanic) is still an open question. Thus, it is expected that the analysis of other Martian areas featuring this kind of landform could shed further light on this issue.

This article focuses on terrain features somewhat similar to those in Figure 1(c), but from a different area of Mars, namely Amazonis Planitia, the relatively young and flat neighboring area west of Olympus Mons aureolae that gives its name to the Amazonian Period of Mars (K. S. Coles et al. 2019). Similar to

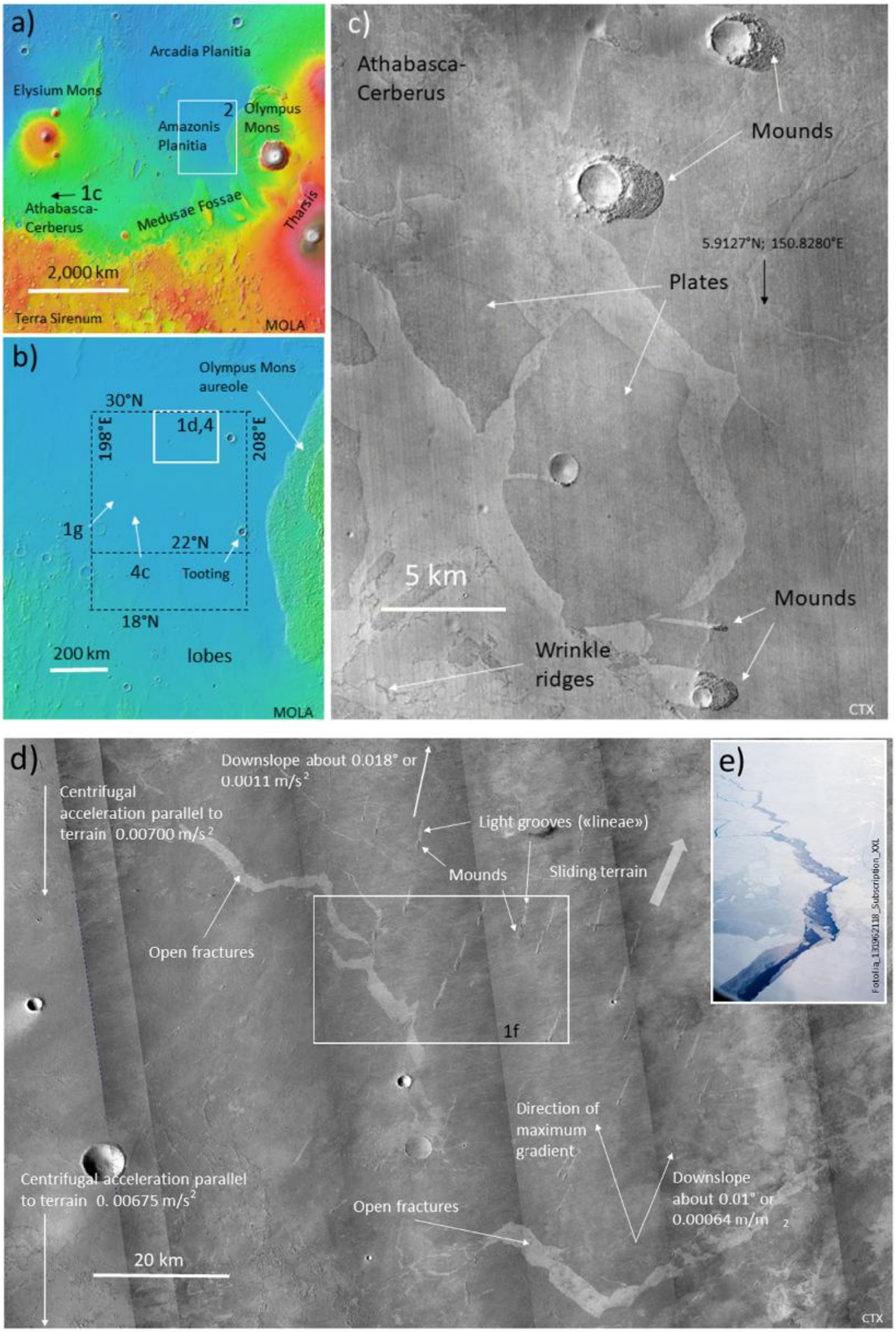

Figure 1. The surveyed area in Amazonis Planitia and an overview of the main topographic features examined in this work. (a) MOLA digital terrain model colorized hillshade map, with the Martian features adjacent to the area. (b) Enlarged MOLA digital terrain model map. (c) Plates in Athabasca–Cerberus. (d) CTX mosaic of the area marked in panel (b), with important features indicated. Shown also are values for the gravitational acceleration parallel to the ground and the centrifugal component of the acceleration. (e) Opening in the Arctic ice pack (Baiterek Media). Reproduced with license. (f) Detail of the area marked in panel (d). Selected MOLA tracks, elevations at some relevant points, and other interesting details are shown. Numbers inside and outside brackets are, respectively, MOLA and HRSC-MOLA blended 200 m DEM version 2. (g) Field of pressure ridges. Note a "ghost crater" that precedes the formation of the mound-groove, as the groove cuts through it. Location in Figure 1(b). In all images of this work, north is pointing up.

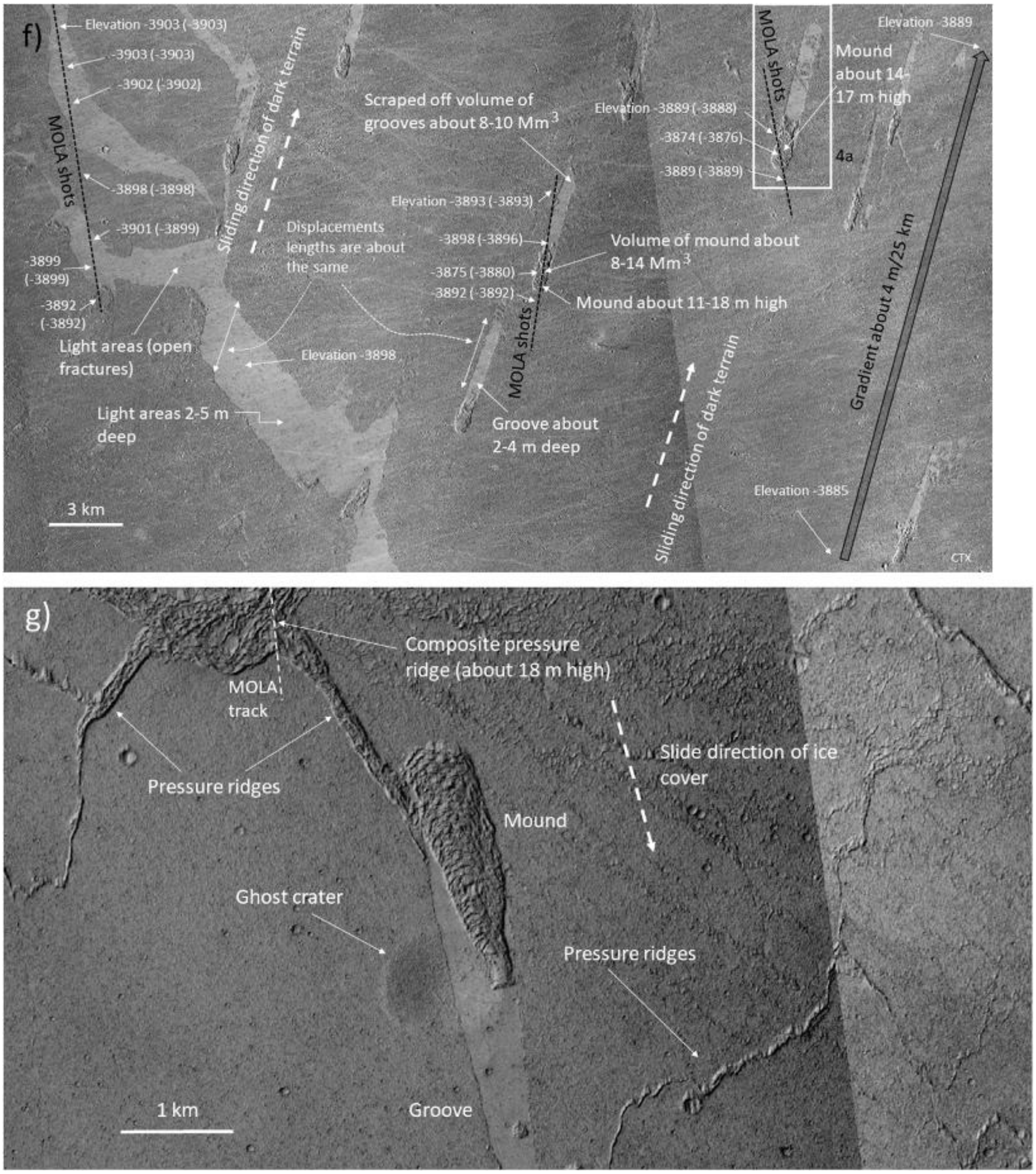

Figure 1. (Continued.)

those of Athabasca–Cerberus, the landforms in Amazonis Planitia also consist primarily of platy terrain where reciprocally dislocated plates are associated with wrinkle ridges, linear scratching features, and other notable morphologies. However, in addition to plates, much wider landscapes of vast terrains (measuring several tens of kilometers) that slid for many kilometers can be observed. Like for Athabasca–Cerberus, the Amazonis Planitia area has been affected by both volcanic processes (it lies near the Tharsis volcanic region) and water processes, since it is positioned at the mouth of an even larger flow area, with the Medusae Fossae formation at its southernmost location. In particular, the area lies at the southern end of the hypothesized Martian ocean (T. J. Parker et al. 2010).

After describing the landforms of Amazonia Planitia in Section 2, Section 3 discusses a possible interpretation (volcanic vs. glacial). Considering the forces required to separate and shift the units, Section 4 will present theoretical calculations aimed at understanding the dynamics of breakage and sliding of the plates and sliding terrains. Finally, a brief discussion and conclusions in Sections 5 and 6 will attempt to assess their nature and history.

2. Observations

2.1. Aspect of the Area and Means of Investigation

Images in this study are based on a Context CTX camera aboard the Mars Reconnaissance Orbiter (M. C. Malin et al. 2007) and HiRISE (A. S. McEwen et al. 2002, 2007), the High-Resolution Stereo Camera (HRSC) aboard Mars Express (G. Neukum et al. 2004), THEMIS aboard Mars Odyssey (P. R. Christensen et al. 2004), and MOLA altimeter data aboard the Mars Global Surveyor mission (D. E. Smith et al. 2001). The area examined within Amazonis Planitia is recent in the Martian geochronology (late Amazonian IAv unit according to K. L. Tanaka et al. 2014). This unit is very smooth and gently sloping, with gradients of 1/1000 or less. Because of the presence of a giant impact crater now nearly filled up by sedimentary deposition in the center of Amazonis Planitia (B. J. Thomson & Head J. W. 2001), the topography reaches its deepest at about 197.°6E, 33.°0N.

For the purpose of the present study, the examined area can be roughly subdivided into three units of increasing latitude, bounded on the west by the meridian passing through longitude 198°E, 159°W and on the east by the aureole of the Olympus Mons aureole, at about 208°E, 150°W. The southern area, between the global dichotomy line at approximately 5°N–10°N and the latitude of about 22°N, is characterized by a constantly descending terrain and a series of thick (50 m or so), wide (100 km), and long (1000 km) lobes that originated at the southern dichotomy and are directed northward. The northern area between 22°N and 30°N, where most of the features documented in this work were found, is characterized by a very smooth terrain, with variations of at most 8 m on a baseline of 2 km. Amazonis Planitia then continues further north for another 5° of latitude on a rough terrain, ending in Arcadia Planitia. The areas of Amazonis Planitia between about 12° and 31°, up to the area west of the W aureole of Olympus Mons (Figures 1(a)–(b)), are characterized by peculiar terrain rich in planar morphologies and are described below.

2.2. Light Grooves ("Lineae") and the Associated Oriented Mounds

The predominantly dark, rugged terrain often opens into distinct, whitish linear units, slightly depressed grooves. Approximately 30 groups of parallel, elongated, light-colored grooves can be recognized in the area (between 2 and 10 in each group). They are tens of kilometers long and oriented primarily toward the N–NE (and less so toward the south). The grooves appear as light tracks on the darker terrain and terminate at one end with a large mound 10–18 m high. Note that mounds belonging to the same furrow field are oriented, that is, they are always located at the same end of each groove (this is the SW end in the specific case of Figures 1(c)–(d)). These features, which curiously resemble cat scratches, can be called "lineae" to conform to a feature name compatible with planetary nomenclature standards, which should be associated with a specific name (e.g., "Amazonis Lineae"). One such cluster is shown in Figure 1(d), and a portion is expanded in Figure 1(f), with key details shown in the figure. A study of the MOLA topographic layers confirms the visual impression that each of these lines is depressed relative to the surrounding darker terrain by approximately 2–5 m, i.e., that they are etched into the otherwise flat area. Unfortunately, the MOLA laser beams intersect only some of the mounds and grooves. Two examples of mounds intersected by MOLA beams are shown in Figure 1(f). The one in the upper right corner of the image shows a maximum mound height of approximately 14–17 m (see elevations reported along the MOLA path). Figure 1(f) also reports the elevations based on HRSC-MOLA blended 200 m digital elevation model (DEM) (version 2), showing only slight differences with respect to the MOLA data. A second example of a MOLA path intersecting both the mound and its corresponding groove is visible in the center of the image. In this case, the mound is approximately 11–18 m high, and the groove is depressed 4–5 m relative to the terrain. Using these data, it follows that the volume scraped from the trench is approximately 8–10 Mm^3, comparable to the volume of the mound, estimated at 8–14 Mm^3. The slightly larger volume of the mound can be attributed to the presence of a hidden obstacle that scraped material from the moving slab. Since the horizontal accuracy of MOLA measurements is approximately 100 m, extrapolation to other lines without MOLA laser points is more problematic. However, assuming a comparable height for all mounds, it follows that the volumes of the mounds are compatible with that eroded from the corresponding groove, indicating that the mounds originate from accumulations of mass scraped from the groove.

2.3. Sliding Terrain Associated with Open Fractures

South of the northernmost groove field, the dark terrain shows large, lighter areas in optical images ("open fractures" in Figure 1(d)). Similar to the light grooves, this terrain also lies 2–5 m beneath the dark terrain, and the length and orientation of the 3–5 km displacement are consistent with the length of the grooves (Figure 1(d)). This indicates that the grooves are the result of sliding along a crust 3–5 km long, meters thick, and tens of kilometers wide, with the displacements of the dark terrain revealing the lighter portions beneath. Oriented grooves are widespread across the analysis area. The distribution of groove groups shows an interesting pattern (Figure 2(a) shows the distribution of grooves and slide terrain in the examined terrain) that will form the basis for the physical analysis in Section 3.1. Figure 2(a), which will be discussed in detail below, schematically shows the distribution and orientation of the rut fields and their association with ground fractures for the most important case shown in Figure 1.

2.4. Pressure Ridges

Figure 1(g) shows examples of sinuous folds traversing the area. These are interpreted as pressure ridges, which typically occur in geological settings dominated by the collision of surface units and are particularly characteristic of sea ice (R. R. Parmeter & M. D. Coon 1972; P. Wadhams 2000). Some of the pressure ridges are several hundred meters wide and can be followed for tens of kilometers. MOLA data show that the ridges are between 5 and 10 m high, with a maximum height reaching about 20 m when composed of multiple ridges.

2.5. Dislocated Plates

Large, shallow plates, separated by even shallower areas, are visible throughout the region. Figure 3 shows an area rich in kilometer-wide plates, each exhibiting relative displacement (Figure 3(a); the MOLA map in panel (c) shows their location). A sketch of the relative motion of selected plates, labeled A–E, reconstructs their rotation-translation from a few hundred meters to kilometers (Figure 3(b)). Note the formation of pressure ridges along the collision lines. Some areas may contain larger plates, on the order of 10 km in diameter, as in Figure 3(d). Note that the plates in Amazonis Planitia are very similar to those in Athabasca (compare Figures 1(c) and 3(a)–(d)).

3. Interpretation

3.1. Suggested Nature of the Terrain in Northern Amazonis Planitia

The landforms described here are interpreted as the result of the instability of an ice sheet overlying a water surface, much

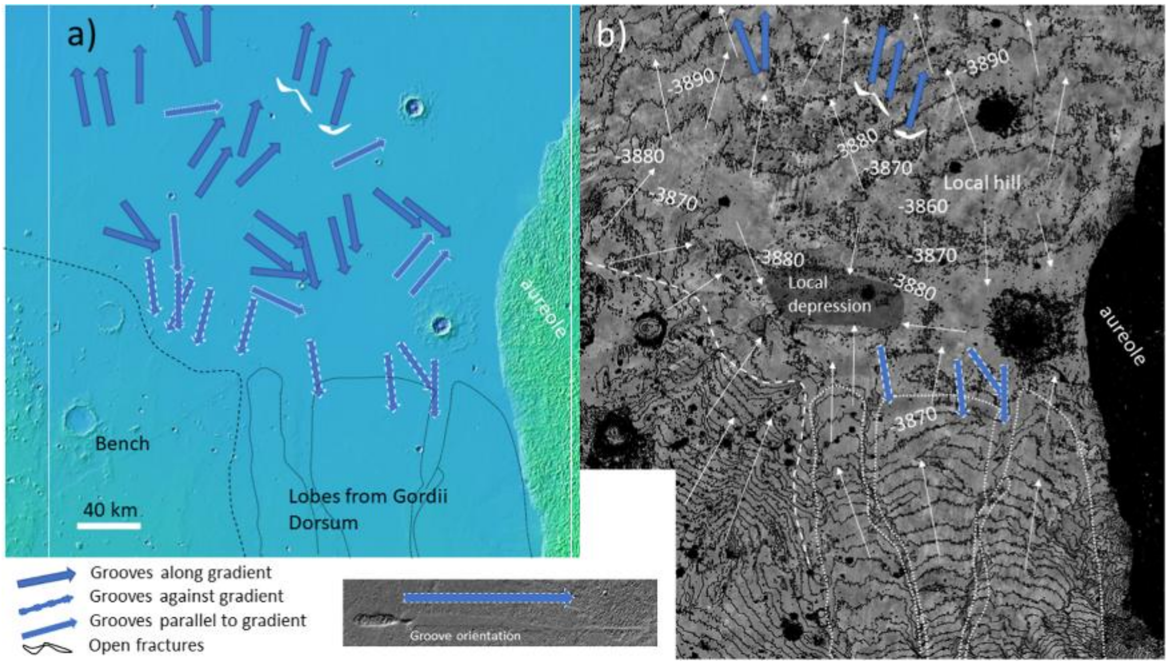

Figure 2. (a) Scheme of the groups of light grooves in the area and their orientation. The groove orientation points as in the image below. Solid arrows indicate groove orientation along the slope gradient; dashed arrows, against the slope gradient; and thin ones, when parallel to slope. The sliding terrain visible in the field in Figure 1 is shown with white lines. (b) Terrain topography for the same area. White arrows at selected points indicate the direction of the local slope gradient. For better visualization, only some of the arrows shown in panel (a) are reported also in panel (b).

like the present-day Arctic Ocean. According to this interpretation, the sliding terrains correspond to the ice sheet's fault lines and resulting ice sheet separation lines, while the grooves result from ice sliding over hard, stable topographic obstacles protruding from the basin floor. The plates are interpreted as smaller ice floes originating from broken ice. This view explains the trough fields in terms of both orientation and length and their association with the slide terrain. The thickness of the ice sheet remnant, on the order of 2–4 m, is comparable to the thickness of the ice in the Arctic Ocean (P. Wadhams 2000). This indicates that even at the peak of glaciation the ice sheet was never thicker than a few meters, implying that the ice was floating freely on water. A further indication of the icy nature of the plates is the irregular surface of terrain outside the grooves (Figure 4). These decametric depressions are irregular in shape and morphologically different from impact craters. Rather, they resemble depressions on ice floes observed in the Arctic Ocean (see, e.g., Figures 2.16–2.17 in P. Wadhams 2000 and recent MOSAiC expedition images[1]). In the Arctic, these depressions are melting pools that form seasonally on ice exposed to the summer atmosphere (P. Wadhams 2000). Similarly, some of the Martian trenches shown in Figure 4 are interpreted as the remnants of melt pools on Martian ice sheets due to prolonged exposure to solar radiation, implying a seasonal radiative temperature above the melting point.

The ice cannot be directly exposed; otherwise, it would rapidly sublimate. Similar to other icy areas on Mars, particularly in the northern reaches of Vastitas Borealis, a layer of wind-borne particles and regolith covering the area could be sufficient to stabilize the ice (e.g., V. Chevrier et al. 2007; see also F. V. De Blasio et al. 2025 and references therein). The presence of ice plates protected by a layer of solid particles has been suggested for other nonpolar areas of Mars, such as the Chaos Terrains (e.g., T. E. Zegers et al. 2010) or Melas Chasma in Valles Marineris (F. V. De Blasio and G. B. Crosta, 2017). Note that the presence of near-surface ice is indicated by radar measurements around the area between the Medusae Fossae formation to the south of the Amazonis Planitia area (J. L. Fastook & J. W. Head 2024; T. R. Watters et al. 2024) and the boundary between Amazonis and Arcadia Planitiae in the north (E. Luzzi et al. 2025), although radar detection of deep ice can be ambiguous (B. Campbell et al. 2008). The presence of subsurface ice in the center of Amazonis Planitia is indirectly confirmed by large impact craters scattered in the area such as the fluidized ejecta of the 28 km wide, recent Tooting crater (P. J. Mouginis-Mark & J. M. Boyce 2012); see Figure 1(b), with its torrents due to ice melting (F. V. De Blasio et al. 2025).

3.2. Relation to Earlier Interpretations

In contrast to the landforms examined here for Amazonis Planitia, which have received little attention in previous work, platy terrains and associated landforms in southwestern Elysium have been described in detail, particularly in the mentioned Cerberus Plains and the Athabasca area south of Elysium Mons. Although the similarity of some landforms between Amazonis Planitia and Athabasca–Cerberus does not necessarily imply the same origin, it is nevertheless likely that at least some of the processes may have been similar, and it is therefore useful to compare platy terrains from the two different areas. J. B. Murray et al. (2005), M. R. Balme et al. (2010), and D. P. Page (2010) interpreted the Elysium–Athabasca landforms (Figure 1(c)) as the product of ice, and M. R. Balme et al. (2013) associated them with water with flows derived from the melting of glacial and periglacial

[1] https://en.highnorthnews.com/science/international-mosaic-arctic-expedition-reaches-north-pole/186394

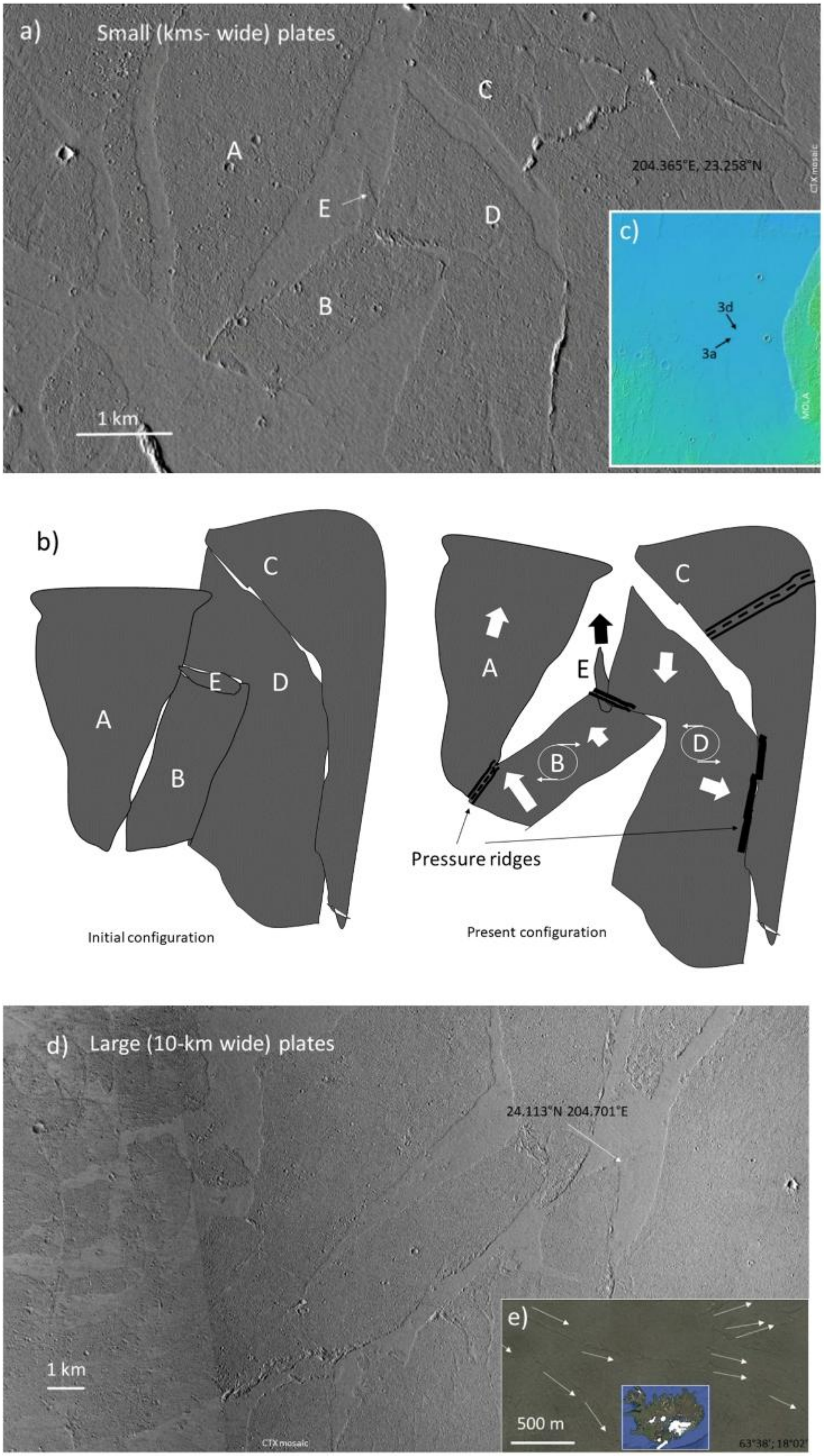

Figure 3. Plates in the study area. (a) Example of small plates. The letters indicate a set of plates whose relative displacement is reconstructed in panel (b) from initial (left) to current configuration (right). Pressure ridges have been created at some of the contacts between the plates. (c) Image positions. (d) Example of a field with larger plates. (e) Lava fields of the Laki volcano in Iceland (reference map below). The arrows indicate some of the grooves produced by the lava flow against protruding obstacles and are oriented along the direction of motion.

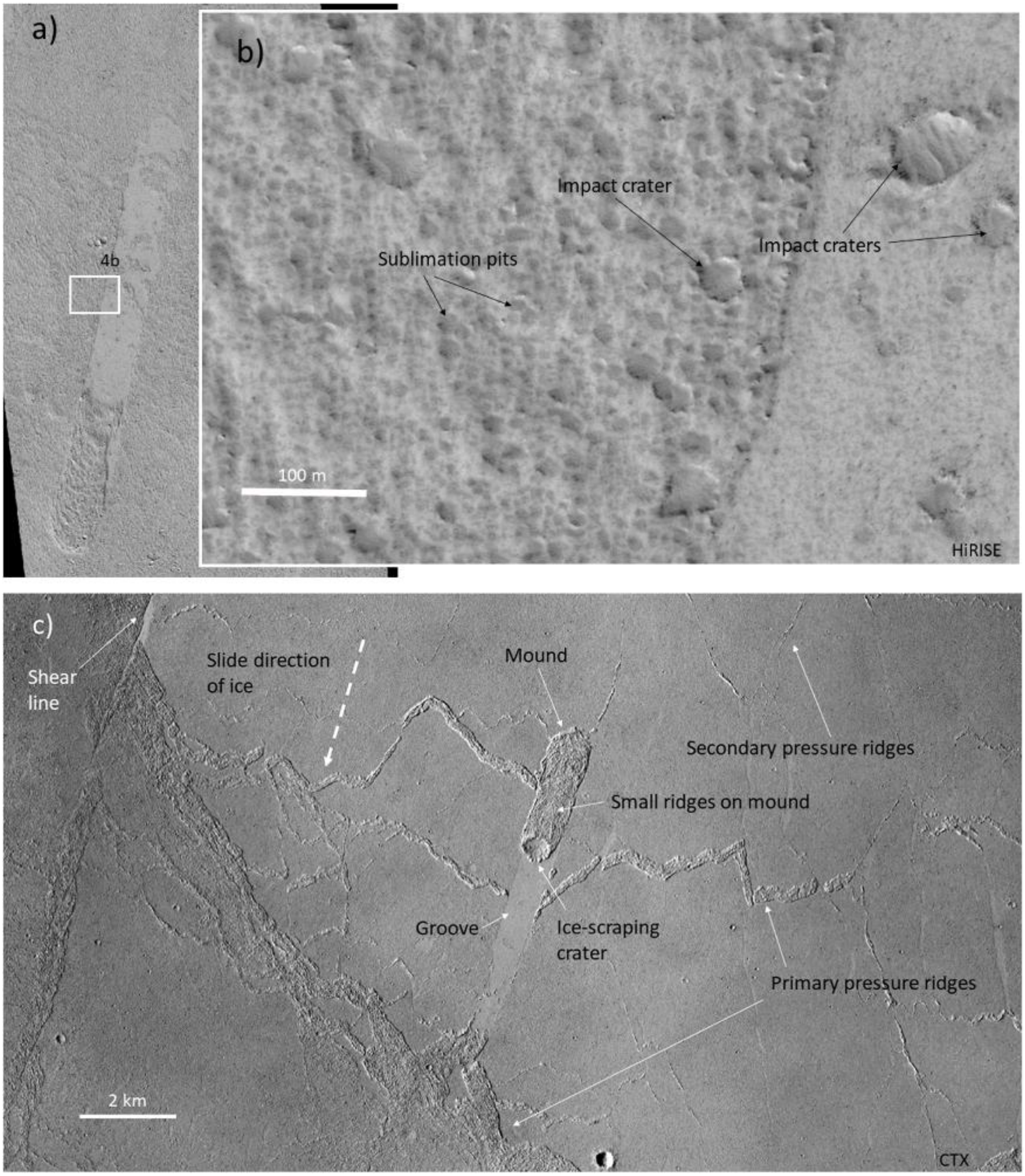

Figure 4. (a) Analysis of the terrain between the light grooves and the dark terrain. (b) HiRISE magnification of the area shows the difference between the terrain of the light grooves, which appears smooth and disturbed mostly by impact craters, and the dark terrain, with numerous pits resembling ice melt pools. (c) In this field full of the interesting features as indicated, a crater responsible for the inception of one groove ("ice-scraping crater") was evidently created before the displacement of the ice blocks occurred.

structures. In particular, the interpretation of the Amazonis Planitia giant plates, suggested here as ice floes floating on water, is essentially the same as that proposed by J. B. Murray et al. (2005) for the Athabasca–Cerberus area. It should be noted, however, that Amazonis Planitia also features the much larger sliding terrains (Figure 1). W. L. Jaeger et al. (2007), L. Keszthelyi et al. (2004), N. A. Cabrol & E. A. Grin (2010), A. J. Ryan & P. R. Christensen (2012), and J. R. Voigt & C. W. Hamilton (2018) favor a volcanic origin for the Athabasca platy terrains and associated landforms. In particular, the giant plates are seen as basaltic crust persisting on molten lava.

Let us consider in more detail a possible volcanic interpretation of the platy terrains of Amazonis Planitia. If the plates are the result of solidified lava, their relative displacement must have occurred above the deeper layer of still-molten lava. The open fractures and associated pairs of grooves-mounds would therefore be the result of the sliding of the resistant basaltic crust against protruding obstacles, rather than of ice. Similarly, grooves-mounds would result from the rubbing of solidified lava against previous craters or other obstacles and the accumulation of solid lava (L. Keszthelyi et al. 2004). Therefore, the grooves and mounds can be explained by both glacial and volcanic scenarios.

However, the volcanic interpretation raises dynamical problems. One of the main ones is that, unlike ice, solid lava is heavier than its melt and would tend to shrink and settle to the bottom during solidification. The plates observed here show no evidence of subsidence and have not struggled with gravitational instability in a low-viscosity fluid. Instead, the evidence (Figure 1) shows that the plates are some meters higher than their melt, as would be expected from the behavior of ice plates. This is essentially the same conclusion drawn by J. B. Murray et al. (2005) for the Athabasca–Cerberus area. Furthermore, such gigantic lava plates have no terrestrial analogs. On Earth, hardened crustal plates like those of Kilauea (D. L. Peck et al. 1979) are much smaller and tend to tip over during solidification owing to their greater density relative to liquidus. A strong argument is also the significant age difference between the plates and adjacent areas (to be discussed in Section 4.4), which is more consistent with the icy rather than basaltic plates.

Regarding the grooves, L. Keszthelyi et al. (2004) compared the Athabasca–Cerberus grooves with those observed in the lava fields at the front of Laki volcano in Iceland, inferring a volcanic nature also for the Martian ones. However, such terrestrial furrows (some of which are shown in Figure 3(e)) were produced by fluid lava against protruding obstacles, while all the grooves documented in the present work, as well as those of Athabasca–Cerberus, were incised on rigid structures (sliding terrain in Amazonis Planitia and plates in Athabasca–Cerberus), and so the terrestrial analog could be misleading. Furthermore, the terrestrial grooves are shorter and narrower than the Martian ones, are more irregular (probably due to partial filling of the groove by fluid lava), and are curved (Figure 3(d)) owing to the nonuniform flow of the lava. In short, the interpretation of the landforms shown in Amazonis Planitia as due to ice rafts on the Martian ocean is considered preferable and is the view supported here. Section 4 will present a physical and quantitative analysis of the forces that caused plate movements in Amazonis Planitia.

3.3. Nature of the Topographic Obstacles

The topographic obstacles responsible for the scraping of ice from the plates and for the creation of groove fields are difficult to identify, as they are themselves buried by ice. They are likely the remnants of small impact crater rims (500–700 m wide). This is confirmed by one of the few locations where the topographic obstacle can be observed. Figure 4(c) shows a crater ("ice-scraping crater") associated with a groove. Because such large craters have a rim height of about 150 m (W. A. Watters et al. 2015), it follows that the water at the time of sliding could not have been deeper than 150 m, and probably even less, as craters formed underwater tend to be flatter (e.g., F. V. De Blasio 2022). One such flat crater ("ghost crater") was shown previously in Figure 1(g).

4. Physical Analysis

4.1. Forces Acting on the Ice Pack and Ice Floes

In this section, the forces causing the displacement of large floes of ice are estimated from the driving and resistive forces acting on the ice during sliding. The mathematical expression and numerical values are presented in Table 1. The gravitational acceleration of a body resting on an inclined plane is $g \sin\beta$, where β is the local slope angle and g is the gravitational acceleration with respect to the center of the planet. This force per unit mass is active only when the ice rests on the ground, and it is canceled when the body floats on the equipotential surface provided by the water. The groove map of Figures 2(a) and (b) shows the direction of the gradient field and level curves in the area. Typical values of the slope $s = \sin\beta \approx \beta$ vary from zero at tops or topographic lows to maximum values of the order of $\approx 10^{-4} - 10^{-3}$ (an average value of $\frac{60\text{ m}}{300\text{ km}} = 2 \times 10^{-4}$ is reported in Table 1) and thus $gs \approx 0.000371 - 0.00371\ \frac{\text{m}}{\text{s}^2}$ with an average slope of $0.00074\frac{\text{m}}{\text{s}^2}$.

Another acceleration term that should be considered, especially when the gravity pull is small, is the centrifugal gradient. The centrifugal acceleration directed radially from the rotation axis of the planet is $a_{\text{centr}} = \frac{4\pi^2 R \cos\Lambda}{T^2} \approx 0.0170 \cos\Lambda\ \frac{\text{m}}{\text{s}^2}$, where $R \approx 3389.5$ km and $T \approx 88{,}642.7$ s are the radius and rotation period of Mars, respectively, and Λ is the latitude (see scheme in Figure 5(a)). Hence, the projection of the acceleration parallel to a meridian on the surface of Mars and directed southward is $f = a_{\text{centr}} \sin\Lambda = -\frac{2\pi^2 R \sin(2\Lambda)}{T^2}$ or $\approx -\ 0.007\ \frac{\text{m}}{\text{s}^2}$ at these latitudes ($\Lambda \approx 30°$), the "minus" sign indicating the southward orientation, i.e., the attraction toward the equator. This force per unit mass varies slowly across the ice pack and therefore acts more or less uniformly. The gradient of this acceleration is $f' = \frac{\partial}{\partial(R\Lambda)}\left(-\frac{2\pi^2 R \sin(2\Lambda)}{T^2}\right) = -\frac{4\pi^2 \cos(2\Lambda)}{T^2} \approx -5.024 \times 10^{-9} \cos(2\Lambda)\ \frac{1}{\text{s}^2}$. Therefore, two points on the same meridian separated by a distance on the surface of the planet of $L \approx 100$ km, corresponding to $\Delta\Lambda \approx 0.03$ rad or $1\overset{\circ}{.}72$ at the present latitudes, would experience a difference in acceleration of $f' \times 100{,}000\text{ m} \approx -2.55 \times 10^{-4}\text{ m s}^{-2}$, or the same order of magnitude as or even greater than the gradient due to inclination of the topographic gradient. The negative sign implies compression of the ice pack due to the centrifugal force between latitudes of 0° and 45° including the area of interest (Figure 5(a)).

The frictional resistance $\mu_{\text{ice}-\text{floor}}$ between the ice and the sea floor is of the order of $\mu_{\text{ice}-\text{floor}} \approx 0.02 - 0.2$ (e.g., A. M. Kietzig et al. 2010), corresponding to forces per unit mass $\mu_{\text{ice}-\text{floor}} \approx (0.02 - 0.2) \times g \approx 0.074 - 0.74\frac{\text{m}}{\text{s}^2}$. Note, however, that even a thin water film lubricating the ice−ice sliding reduces the friction by at least one or more orders of magnitude (e.g., A. M. Kietzig et al. 2010; L. Makkonen & M. Tikanmaki 2014). A thicker layer (millimeters to centimeters or more) can reduce friction to a virtually negligible hydrodynamical shear resistance (G. K. Batchelor 2000). Note that even for pure ice the friction coefficients are uncertain owing to its significant dependence on temperature, velocity, and ice crystal size (A. M. Kietzig et al. 2010), so we cannot be quantitatively precise in the estimates. Let us consider the forces at play when an opening of width W is created on the ice pack of thickness H inclined at an angle β. The force required to break this chunk is $-\tau_{\text{tens}} WH$. The gravity pull acting on this ice portion will be $WHM \sin\beta g\ \rho$, where M is the length of the disturbance, and so if we neglect the effect of the resistance exerted by topographic obstacles at the grooves (to be considered in Section 4.2), the ratio of resistance to gravity is

$$\eta = \frac{\tau_{\text{tens}}}{\rho g \sin\beta\ M}. \tag{1}$$

Table 1
The Data Used for the Calculation of the Displacement Forces Acting on an Ice Floe

Forces per Unit Mass, $\frac{\mathrm{m}}{\mathrm{s}^2}$	Gravity Pull along Slope	Centrifugal Component Parallel to Surface Gradient	Centrifugal Forces through Ice Pack along a Distance of 100 km	Friction When Sliding on Oceanic Floor (Water Absent)	Friction When Sliding on Ice	Tensile break at the rear of the ice chunk	Force Exerted by Craters Rims and Producing the Grooves
Expression or symbol	$g \sin\beta$	f	$f' \times R\Delta\Lambda$	$g\ \mu_{\mathrm{ice-floor}}$	$g\ \mu_{\mathrm{ice-ice}}$	$\frac{\tau_{\mathrm{tens}}}{\rho M}$	$500MN \times \frac{\pi D(\mathrm{m})}{2} \frac{1}{300\ \mathrm{m}} \times \frac{H}{H_{\mathrm{Arctic}}} \times \frac{1}{QHL\rho}$ (for 1 crater)
Direction	Pointing toward topographic lows	Toward S	Tends to compress the ice floes at the latitudes of interest ($0° - 45°$)	Against the direction of movement	Against the direction of movement	Against the direction of pull	Against the direction of movement
Order of magnitude of the forces per unit mass in Amazonis Planitia, $\frac{\mathrm{m}}{\mathrm{s}^2}$	7.4×10^{-4}	7×10^{-3}	2.5×10^{-4}	0 (if water layer still present), $(0.02–0.2) \times g_{\mathrm{MARS}} = 0.074 - 0.74$ (water layer absent)	$(0.02–0.2) \times g_{\mathrm{MARS}} = 0.074 - 0.74$	0.002	$0.005 - 0.01$
Period of activity	When the ocean water has vanished and the ice rests on the sea floor	Always active	Always active	When the ocean water has vanished and the ice rests on the sea floor	Active only on the portions overriding the ice	Active before ice rupture	When a topographic accident is present

Note.
The numerical values are obtained with $\sin\beta \approx 0.00025$ or $\beta \approx 0.014°$; $\tau_{\mathrm{tensile}} \approx 1$ MPa; $\tau_{\mathrm{compressive}} \approx 5$ MPa; $\tau_{\mathrm{strength}} \approx 30$ MPa; $\rho \approx 920$; $H = 1$ m; $L = 4$ km; $W = 40$ km; $M \approx 50$ km. The acceleration away from the planet's axis is $a_{\mathrm{centr}} = \frac{4\pi^2 R_M \cos\Lambda}{T_M^2} = 0.0171 \quad \cos\Lambda\ \frac{\mathrm{m}}{\mathrm{s}^2}$.

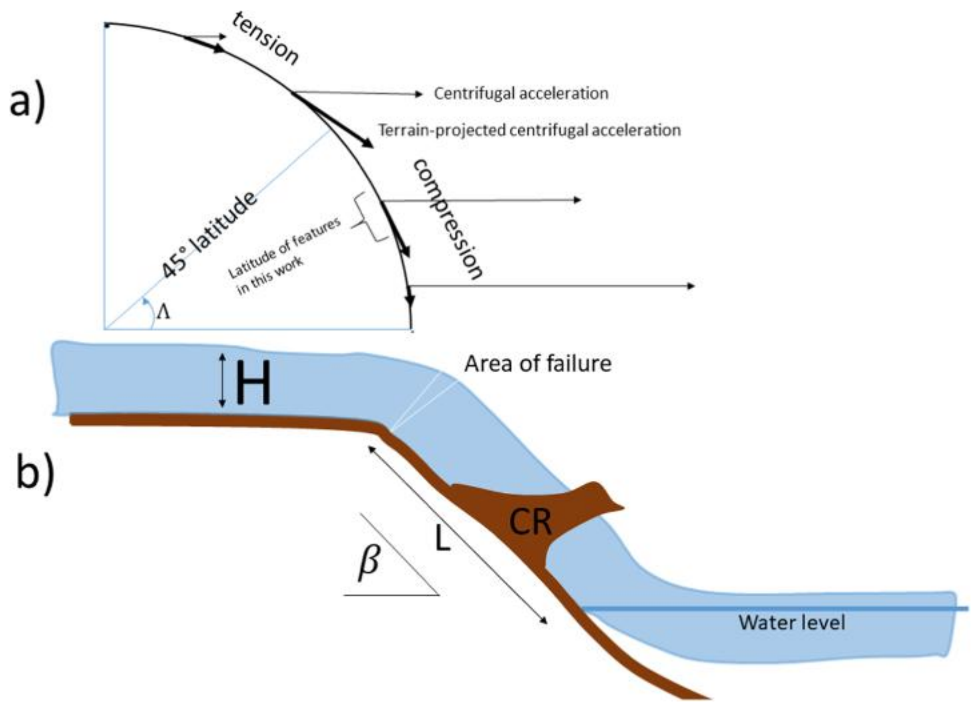

Figure 5. (a) Centrifugal accelerations acting on the ice floes due to the rotation of Mars when floating on an equipotential surface. The latitude range of the features examined in this work is less than 45°, where ice on the surface is compressed by the planet's rotation. (b) Scheme for the calculation of the ice pack breakup criterion (see text).

The tensile strength of sea ice depends on several variables, including temperature, porosity, and grain size (E. M. Schulson & P. Duval 2009). Considering these uncertainties, we expect values of the order $\tau_{\text{tens}} \approx 0.1 - 1$ MPa (J. R. Richter-Menge & K. F. Jones 1993; J. J. Petrovic 2003; E. M. Schulson & P. Duval 2009; G. W. Timco & W. F. Weeks 2010) and $\rho g \sin\beta \approx 0.71$ Pa m^{-1}, and using $M \approx 100$ km and $\sin\beta \approx 10^{-3}$, it follows that $\eta \approx 0.28$–1.8, indicating the plausibility of the above instability scenario.

Most of the ice displacements, as indicated by the direction of the groove fields, took place along the slope (arrows in Figure 2(a)). Such along-slope displacements can thus be interpreted as arising from the effect of local gravity. Since an ice floe floating on water is on an equipotential surface, it is suggested that the downslope movement of the ice floes was triggered by the contact between the ice floes and the floor of a declining ocean. At that time, water was still present, not enough to create an equipotential surface, and nevertheless sufficient to lubricate the contact between ice floes and the floor (Figure 5(b)). Some groove fields, however, indicate a force acting against the local slope (dashed arrows in Figure 2(a)). Note that these against-slope grooves are mostly directed toward the south, indicating that they may have been triggered by centrifugal forces having the same direction. The centrifugal force acts also on the equipotential surface and in the absence of contact with the ocean floor, and therefore these displacements could have occurred when the ocean was still present but had a reduced depth, since obstacles were capable to create the groove.

4.2. Mechanics of Groove Formation upon Ice Pack Dislocation

We now estimate the mechanics of groove development more quantitatively. The impact force of sea ice floes against artifacts in the Arctic has been recorded in detail. Forces of the order of 500 MN have been reported, for example, for the Molikpaq platform (base dimensions approximately 100 m × 100 m) in the Canadian Beaufort sea, while an average of 3 MN was measured around the 5 m diameter Nordstromsgrund lighthouse with ice drifting at a speed of 1 m minute^{-1} (S. Løset et al. 2006). These figures would correspond to a stress of about $500\frac{\text{MN}}{300\text{ m}\times 1\text{ m}} \approx 1.7$ and 0.4 MPa, respectively (for a nominal ice thickness of 1 m), which, with all caveats in such rough estimates, slightly exceed the tensile strength of ice (0.1–1 MPa; E. M. Schulson & P. Duval 2009), hence explaining why the ice was torn apart. Proportionally lower stresses result from ice thicker than 1 m. Rescaled to Mars on a crater of diameter D, the force would be approximately $\Phi \approx 500\text{ MN} \times \frac{\pi D\text{ (m)}}{2}\frac{1}{300\text{ m}} \times \frac{H_{\text{Mars}}}{H_{\text{Arctic}}}$, assuming that the perimeter responsible for the ice tearing has a length of $\frac{\pi D\text{ (m)}}{2}$ to compare with the 300 m of the sum of the sides of the platform (note that the compressive forces will be larger than the shear forces, and thus the sides of the crater will contribute differently from the front, but here we only consider orders-of-magnitude estimates). With a crater diameter of 500 m and a comparable ice thickness ($\frac{H_{\text{Mars}}}{H_{\text{Arctic}}} = 1$), the estimate would yield values slightly higher than those recorded in the Arctic, or of the order of $\Phi \approx 500 - 1000$ MN. The groove fields shown in Figure 1 indicate the presence of a crater approximately every 200 km^2, or crater density $\# = 5\times 10^{-3}$ km^{-2}= 5×10^{-9} m^{-2}, and hence the resistance force per unit mass exerted by such craters on the entire slab would be approximately $\frac{500 - 1000\text{ MN}}{H_{\text{mars}}\times 200\text{ km}^2\times\rho} \approx 0.0025 - 0.005\frac{\text{m}}{\text{s}^2}$.

4.3. Instability of the Ice Pack

In addition to the craters pinning the ice cap at the crater locations, the stability condition of the ice pack should include that part resting on a horizontal area ("local hill" in Figure 2). Referring to Figure 5(b), the area of failure of the ice pack will materialize at the slope break with the local hill, and therefore, as a generalization of Equation (1), the break length L should be at least

$$L > \frac{\tau_{\mathrm{tens}}/\rho g}{\sin\beta - \mu\cos\beta - \frac{\Phi\#}{\rho g\, H}}. \qquad (2)$$

Thus, if the denominator of Equation (2) is positive, a drop in the water level will increase the instability over time since, from the simple geometry of Figure 5(b), the length L will increase and inequality (2) will be satisfied. While the numerator of Equation (2) is about 30 m or more, the denominator results from a balance between slope, on the one hand, and friction plus the pinning effect of craters, on the other, which contribute with opposite signs. In fact, even assuming $\mu \approx 0$ for simplicity, both the slope and the term $\frac{\Phi\#}{\rho g\, H}$ are of the order of 10^{-4}. If the pinning force is large ($\frac{\Phi\#}{\rho g\, H} > \sin\beta$), the slab is stable, which means that the opposite condition must have occurred, $\frac{\Phi\#}{\rho g\, H} < \sin\beta$. However, it is difficult to determine the contributions to the denominator of Equation (2) since, as shown above, the individual addenda have a large uncertainty and may change by a large factor ($\sin\beta$ can change between $\approx 10^{-4}$ and 10^{-3} as seen earlier, and $\frac{\Phi\#}{\rho g\, H}$ is even more uncertain). Since the denominator is the difference in contributions of the order 10^{-4}, it will be itself of that order, which would give a fraction of 300 km for the instability of the ice pack, a figure compatible to the hundred-kilometer length of the ice pack that slid. Thus, we conclude that the order-of-magnitude estimates indicate that the groove fields in Amazonis Planitia documented in this work are compatible with the model of ice rip-apart that created them in correspondence with craters protruding from the sea floor.

4.4. Impact Craters and Timing of Groove Formation

In principle, the age of undegraded Martian terrains can be inferred from crater counts (G. G. Michael & G. Neukum 2010). However, the extremely small areas of the sliding terrains a, each one of the order of only $a \approx 70 - 100\ \mathrm{km}^2$, imply the absence of large craters, as shown below. Indeed, for terrains dating between 500 Ma and 2 Ga (considered as ages ranges for Amazonis–Arcadia Planitiae), the cumulative frequency per square kilometer for craters greater than 1 km is between $2 \times 10^{-4}\ \mathrm{km}^{-2}$ and $10^{-3}\ \mathrm{km}^{-2}$ (e.g., W. K. Hartmann & G. Neukum 2001). Thus, over an area of $70\ \mathrm{km}^2$, one might expect about 0.014 and 0.07 craters larger than 1 km for these two ages. Their absence in the sliding terrains is thus reasonable, making it difficult to accurately determine the absolute time of formation of the sliding terrain without Poisson statistical corrections.

To estimate the degree of error, we compare the age determination for the "dark" terrain on a small area and the one for a much larger area $A = 177,152\ \mathrm{km}^2$ (tens of craters larger than 1 km should be present over such a large area) using the crater counting tool integrated in JMARS (P. R. Christensen et al. 2009) and the statistical analysis of the software "CraterstatsII" for age estimation (G. G. Michael & G. Neukum 2010). The chronology and production functions for the analysis are, respectively, the ones by G. Neukum et al. (2001) and B. A. Ivanov (2001). The results for the large area are shown in Figure 6(c). Note that the number of craters tends to an isochrone of about 1 Ga, which is much older than the age estimation of the smaller area "DA" of the dark terrain shown in Figure 6, which gives 150 Ma. While the age of the sliding terrains is difficult to determine, it is suggested that the age difference between the sliding terrain and the adjacent darker areas can be estimated if the areas are of similar extent. Figure 6 shows the results for the light areas corresponding to the sliding terrains named "GT-1", "GT-2," and "GT-3." Craters larger than 60 m were measured in the selected areas. Clustering due to secondary impacts and to asteroids breaking up in the atmosphere was only minimal. Figure 7 shows the results of the statistical analysis based on crater counts indicating ages of 21, 23, and 50 Ma for the three areas. While the similarity between the ages of areas GT-1 and GT-2 indicates an almost concomitant ice slab sliding event, the significantly higher age of 50 Ma of area GT-3 indicates an earlier age of the sliding event. Therefore, the ice pack sliding process lasted for a time interval of at least several tens of millions of years. The darker terrain (area "DA") yielded the mentioned age of about 150 Ma. In fact, the older age of the darker areas can be appreciated by visually examining the terrain (Figure 6(b)). The age differences therefore confirm the narrative of an ice pack that slid and opened as a consequence of external forces, the difference of about 100–130 Ma between the dark areas and the lighter sliding terrains indicating the time of the initial sliding of the ice pack, therefore datable with all the appropriate caveats to about 870–900 Ma.

There are at least two important issues with the impact craters on the dark areas. First, note that craters larger than about 200 m are smooth and have irregular rims (Figure 7(a)), which is indicative of severe creep deformation. This may indicate degradation of the larger craters by plastic deformation, a phenomenon well documented on icy Mars, particularly on polar deposits (P. Thomas et al. 1992; N. Mangold et al. 2002; A. V. Pathare et al. 2005). More importantly, according to the present narrative, many of the impact craters on the dark terrain (which is what remains of the ice crust) were produced when the pack ice was still floating on the ocean. Under these circumstances, the crater-producing meteoroid pierced through the meters-thick ice layer. Experiments with projectiles fired at much smaller scale but at comparable meteoroid velocities indicate that when the impactor is much larger than the thickness of the ice layer floating on the water, the crater is comparable in size to the diameter of the impactor. However, when the ice is not floating, the resulting crater is much larger than the impactor diameter (I. D. Grey & M. J. Burchell 2003). A double population of craters could therefore form on dark terrains, one formed in an early phase of floating ice when meteoroids created craters of their size, and one formed after the ocean disappeared, with craters much larger than the impactor diameter. This peculiar distribution of crater sizes would also contribute to the paucity of large craters and would also influence the crater count statistics presented in Figure 6. At present, it is unclear how to distinguish between

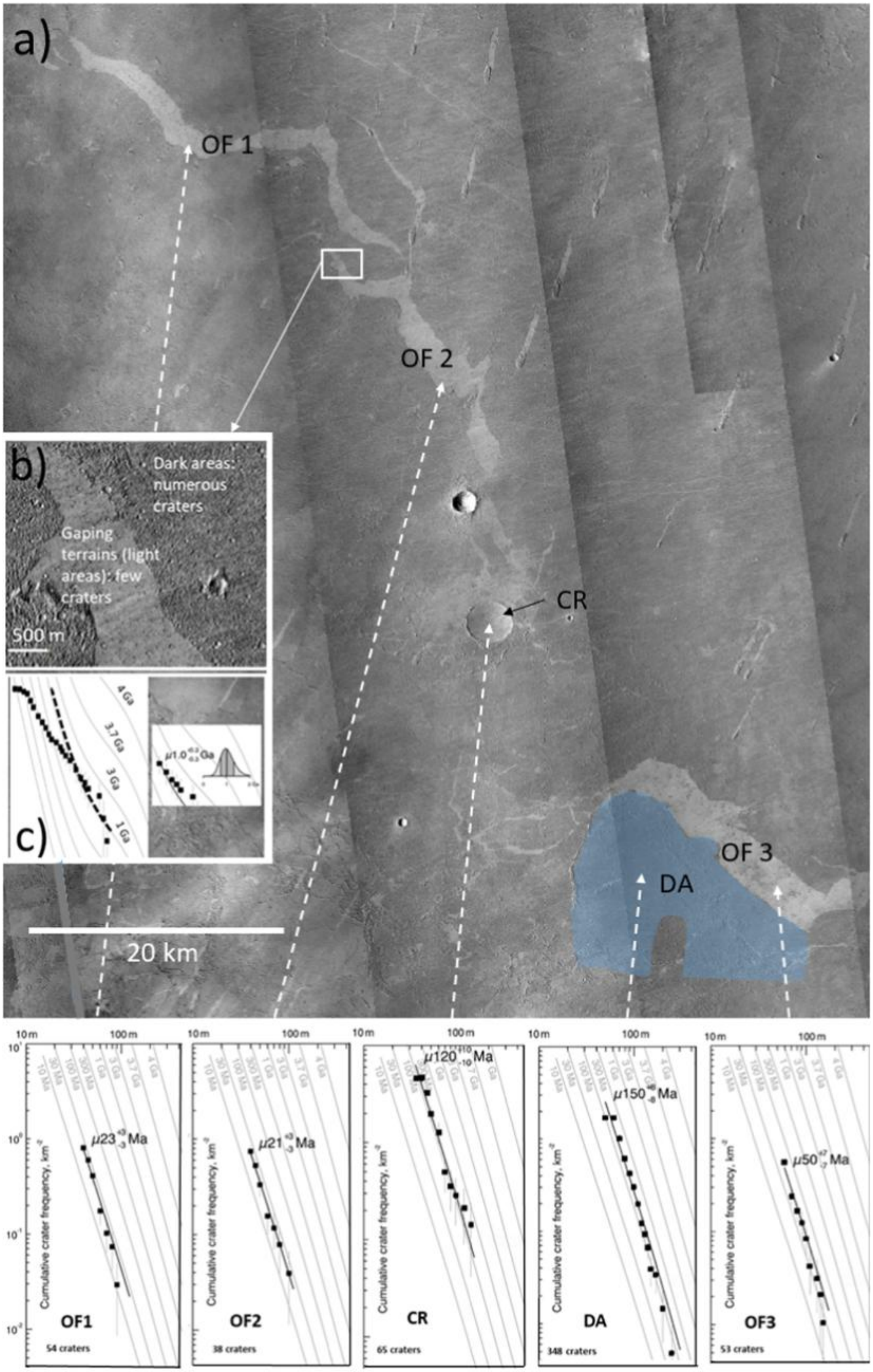

Figure 6. (a) Crater size analysis for five selected areas: light areas of open fractures (OF1, OF2, OF3), dark area (DA), and the inside of the large crater visible in the figure (CR). Panel (b) shows a magnification of the area in the white square (top), and panel (c) shows the crater count for the whole area, including the largest craters, providing an age of 1 Ga.

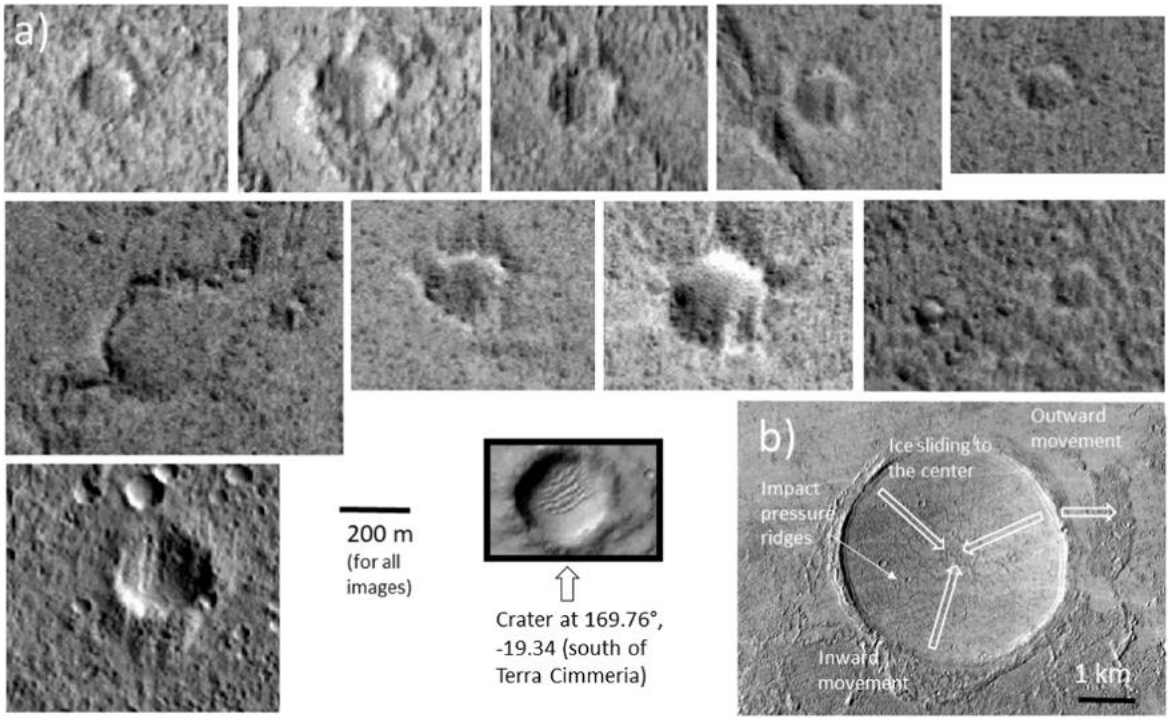

Figure 7. (a) Selected examples of 150–350 m wide, degraded craters in the study area. The crater in the center of the figure is an example from the ancient area of Terra Cimmeria (and thus not incised on the ice pack) and is shown for comparison. (b) A large crater from before the ocean disappearance ("CR" in Figure 6).

the two types of craters, and the question is open to future investigations.

4.5. Indications from Craters Predating Ice Cap Instability

The scenario is supported by the observations on craters that predate breakup of the ice pack. These can be recognized by their low elevation, the infilling by sediments, and, as shown here, their influence on the ice. A notable example is a large 4 km diameter crater (Figure 7(b)) that was created by the impact of a meteoroid against the sea floor. The older age of the ice on the surface of the crater ("CR" in Figure 6; 120 Ma result from crater counting) is comparable to that for the dark terrain in the same area and confirms that the surface was always covered by the ice. When the ice sheet came in contact with the rims and flanks of the crater, the ice outside the rim slid outward (Figure 7(b)), while the ice inside the crater slid toward the center, thus creating a polygonal terrain by compression. Another interesting crater is the one shown earlier in Figure 1(g). This 1 km wide crater was formed before the breakup of the ice pack (it is, in fact, incised by one of the light grooves). Note the very smooth rim, probably a consequence of redistribution of sediments in the oceanic environment.

5. Discussion

5.1. Relation to the Putative Martian Ocean

The past existence of the long-life ocean of Mars, termed the "Oceanus Borealis," has been hypothesized to explain a series of features in the northern hemisphere, in particular, but not exclusively, the peculiar flatness of the northern lowlands (B. K. Lucchitta et al. 1986; J. Brandenburg 1987; V.R. Baker et al. 1991; T. J. Parker 1994; V.R. Baker et al. 2000; S. M. Clifford & T. J. Parker 2001; M. H. Carr & J. W. Head III 2003; M. H. Carr 2006; T. J. Parker et al. 2010). Determining the existence of the putative ocean is fundamental to reconstructing the geomorphological and climatic history of Mars and is a prerequisite for any search for possible life-forms on ancient Mars (e.g., T. J. Parker et al. 2010). Numerous studies of the ancient Martian ocean, however, have not clarified whether the ocean was long-lived or, rather, was the ephemeral remnant of water masses in the northern lowlands, due to catastrophic discharges from outflow channels (V. R. Baker et al. 1991).

Many works have focused on paleoshorelines as possible evidence for the existence of the ocean, but the positive correlation has been questioned (e.g., M. C. Malin & K. S. Edgett 1999; T. J. Parker et al. 2010). Other works have hypothesized the presence of large amounts of water on ancient Mars to interpret specific landforms attributable to the ocean floor; for example, recent studies of putative tsunami deposits on Mars would confirm the presence of a vast past ocean (J. A. Rodriguez et al. 2016; F. V. De Blasio 2020). The present work focused on a set of landforms that strongly suggest an ice-covered vast water surface comparable to the Arctic ice pack, which would imply the presence of a past ocean floor. The evidence has been supported by images and calculations indicating the presence of sea ice over large pools of water in Amazonia Planitia. Since Amazonia Planitia has its minimum elevation at about −4000 m below the reference level, the area considered lies below the levels suggested for the ancient Oceanus Borealis (T. J. Parker et al. 2010) and is therefore considered among the areas bathed by the ancient ocean. The ice crust, however, was unstable, and this work has documented extensive sea ice pack displacements.

5.2. Inferred Timing of Ice Failure

To summarize, the images, physical estimates, and age measurements of the sliding terrains support a succession of

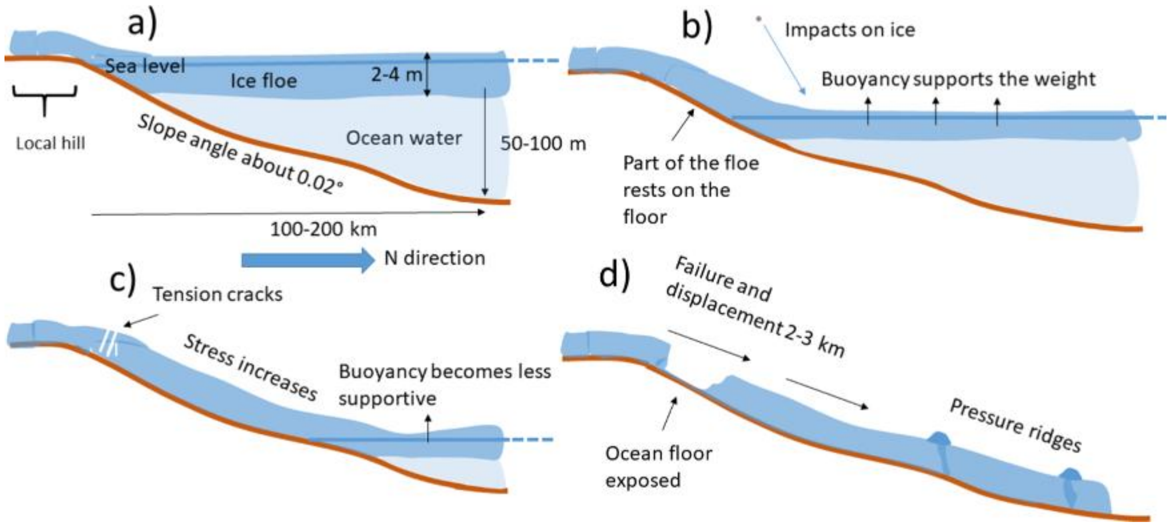

Figure 8. Formation of the sliding terrain due to ice pack instability. In panel (a) the water is retreating and one part of the ice floe (left) rests on a higher area ("local hill"), while the part on the right still floats on the water. As the ocean retreats (panel (b)), the tension across the ice crust grows (panel (c)) until failure occurs (panel (d)) and the ocean floor is exposed, which corresponds to observed terrain sliding due to gravity.

events like the one shown in Figure 8. The figure sketches the evolution of the area where the northern sliding of the ice cap took place (Figures 1(c) and (d)). In panel (a) the ocean is already on the way to disappearance from its deepest levels on Mars that were reached much earlier in the late Hesperian. The southernmost part of the ice cap is resting on the area of the "local hill" also visible in Figure 1. As the ocean shrinks further on the way to its irreversible loss, the ice cover decreases height (panel (b)), and stress builds up along the ice resting on the slope, due to loss of buoyancy on part of the ice floe, shown on the right of panel (c). When the stress grows further, reaching the critical tensile strength of about 0.1–1 MPa, failure takes place (panel (d)). The open fractures correspond to the area where the ocean floor was exposed. As discussed, craters present at the sea floor may increase stability by buttressing the ice pack, but this is not shown in the scheme for simplicity.

Finally, note that the age difference between the dark and light terrains (open fractures) cannot be explained in the volcanic model, according to which the plates would have solidified just slightly earlier than the melt, i.e., after geologically insignificant times, and thus they should mark the same age. The age difference can be more easily explained in the ice interpretation according to which the separating areas, being the remnant of the sea floor, were exposed when the plates separated and should thus be younger than the dark terrains. A younger age compared with the surrounding terrain was found also for the plates in Athabasca (J. B. Murray et al. 2005), leading to the same conclusion drawn here of incompatibility with the volcanic scenario (D. P. Page 2010).

6. Conclusions

This work documented a series of landforms in Amazonis Planitia on Mars consisting in grooves-mounds associations, vast masses of sliding terrain, displaced plates, and meandering wrinkles explained as pressure ridges. Similar to the neighboring area Athabasca–Cerberus, where plates were regarded as ice blocks floating on a large lake, these landforms have been interpreted as the remnants of a vast ice pack often broken up into floating ice floes. The vastity of the area suggests that, rather than a lake, the water surface was that of the ancient Martian ocean, hypothesized by many researchers. When the ocean was a few hundred meters deep, the ocean surface was locally equivalent to an equipotential surface, so that the ice pack was not gravitationally disturbed by interaction with the ocean floor. During this phase, cracking and southward sliding of ice occurred sporadically, as a consequence of the weak centrifugal potential. As the ocean receded, the ice pack approached the ocean floor, and the topography began to play a role. The observed ice breakup patterns indicate a progressive accumulation of stress on the vast equatorial ice pack as the ice in contact with the ocean floor began to slide, driven by the slope gradient. The dark areas discussed in this work are interpreted as the remnants of the ice sheet on the surface of the ancient Martian ocean, while the lighter, open fractures with fewer craters represent a window onto the previously ice-protected ocean floor exposed by the breakup-slide event. The different ages of the two surfaces support this scenario, while they are incompatible with volcanic processes. The grooves-mounds landforms associated with sliding terrains were produced when the ice slid on topographic obstacles.

In short, the scenario may capture the phase of the gradually waning equatorial Martian ocean covered by some meters-thick ice sheet very similar to the Arctic Ocean. The timing of these events indicates that the sliding and breakup activity of the ice pack cracking lasted at least several tens of millions of years.

Acknowledgments

This paper was partially funded by Ateneo-Quota Competitiva 51893 (Lakes on Mars), Università di Milano–Bicocca.

ORCID iDs

Fabio Vittorio De Blasio https://orcid.org/0000-0003-1291-0565

References

Baker, V. R., Strom, R. G., Dohm, J. M., et al. 2000, Mars-Oceanus Borealis, Ancient Glaciers, and the MEGAOUTFLO Hypothesis, LPSC, 31, 2000
Baker, V. R., Strom, R. G., Gulick, V. C., et al. 1991, Ancient Oceans, Ice Sheets and the Hydrological Cycle on Mars, Natur, 352, 589

Balme, M. R., Gallagher, C., Page, D. P., et al. 2010, 10–The Western Elysium Planitia Paleolake, Lakes on Mars (Elsevier), 275
Balme, M. R., Gallagher, C. J., & Hauber, E. 2013, Morphological Evidence for Geologically Young Thaw of Ice on Mars: A Review of Recent Studies Using High-Resolution Imaging Data, PrPG, 37, 289
Brandenburg, J. 1987, The Paleo-Ocean of Mars, in MECA Symp. on Mars: Evolution of Its Climate and Atmosphere (Lunar and Planetary Inst.), 20
Batchelor, G. K. 2000, An Introduction to Fluid Dynamics (Cambridge Univ. Press)
Brackenridge, G. R. 1993, Modern Shelf Ice, Equatorial Aeolis Quadrangle, Mars, LPSC, 24, 175
Cabrol, N. A., & Grin, E. A. 2010, Searching for Lakes on Mars: Four Decades of Exploration, in Lakes on Mars, ed. N. A. Cabrol & E. A. Grin (Elsevier)
Campbell, B., Carter, L., Phillips, R., et al. 2008, SHARAD Radar Sounding of the Vastitas Borealis Formation in Amazonis Planitia, JGRE, 113, E12010
Carr, M. H. 1996, Water on Mars (Oxford Univ. Press)
Carr, M. H. 2006, The Surface of Mars (Cambridge Univ. Press)
Carr, M. H., & Head, J. W., III 2003, Ocean on Mars: An Assessment of the Observational Evidence and Possible Fate, JGRE, 108, 5042
Chevrier, V., Sears, D. W., Chittenden, J. D., et al. 2007, Sublimation Rate of Ice under Simulated Mars Conditions and the Effect of Layers of Mock Regolith JSC Mars-1, GeoRL, 34, L02203
Christensen, P. R., Engle, E., Anwar, S., et al. 2009, JMARS-a Planetary GIS, AGUFM, IN22A–06
Christensen, P. R., Jakosky, B. M., Kieffer, H. H., Ravine, M., et al. 2004, The Thermal Emission Imaging System (THEMIS) for the Mars 2001 Odyssey Mission, SSRv, 110, 85
Clifford, S. M., & Parker, T. J. 2001, The Evolution of the Martian Hydrosphere: Implication for the Fate of a Primordial Ocean and the Current State of the Northern Plains, Icar, 154, 40
Coles, K. S., Tanaka, K. L., & Christensen, P. R. 2019, The Atlas of Mars: Mapping Its Geography and Geology (Cambridge Univ. Press)
De Blasio, F. V. 2020, Frontal Aureole Deposit on Acheron Fossae Ridge as Evidence for Landslide-Generated Tsunami on Mars, P&SS, 187, 104911
De Blasio, F. V. 2022, The Large Dendritic Morphologies in the Antoniadi Crater (Mars) and Their Potential Astrobiological Significance, Geosc, 12, 53
De Blasio, F. V., Caccia, A., & Crosta, G. B. 2025, Transient Hydrology in Amazonis Planitia (Mars) in the Aftermath of the Tooting Impact, JGRE, 130, e2024JE008915
De Blasio, F. V., & Crosta, G. B. 2017, Modelling Martian Landslides: Dynamics, Velocity, and Paleoenvironmental Implications, EPJP, 132, 468
Fastook, J. L., & Head, J. W. 2024, Origin of Ice in the Medusae Fossae Formation, Equatorial Mars, Icar, 421, 116226
Grey, I. D., & Burchell, M. J. 2003, Hypervelocity Impact Cratering on Water Ice Targets at Temperatures Ranging from 100 K to 253 K, JGRE, 108, 5019
Hartmann, W. K., & Berman, D. C. 2000, Elysium Planitia Lava Flows: Crater Count Chronology and Geological Implications, JGR, 105, 15011
Hartmann, W. K., & Neukum, G. 2001, Cratering Chronology and Evolution of Mars, SSRv, 96, 165Cratering Chronology and Evolution of Mars
Ivanov, B. A. 2001, Mars/Moon Cratering Rate Ratio Estimates, SSRv, 96, 87
Jaeger, W. L., Keszthelyi, L. P., McEwen, A. S., Dundas, C. M., & Russell, P. S. 2007, Athabasca Valles, Mars: A Lava-Draped Channel System, Sci, 317, 1709
Keszthelyi, L., Thordarson, T., McEwen, A., et al. 2004, Icelandic Analogs to Martian Flood Lavas, GGG, 5, Q11014
Kietzig, A. M., Hatzikiriakos, S. G., & Englezos, P. 2010, Physics of Ice Friction, JAP, 107, 081101
Leverington, D. W. 2018, Is Kasei Valles (Mars) the Largest Volcanic Channel in the Solar System?, Icar, 301, 37
Løset, S., Shkhinek, K. N., Gudmestad, O. T., & Høyland, K. V. 2006, Actions from Ice on Arctic Offshore and Coastal Structures (LAN), 53
Lucchitta, B. K., Ferguson, H. M., & Summers, C. 1986, Sedimentary Deposits in the Northern Lowland Plains, Mars, JGR, 91, 166
Luzzi, E., Heldmann, J. L., Williams, K. E., et al. 2025, Geomorphological Evidence of Near-Surface Ice at Candidate Landing Sites in Northern Amazonis Planitia, Mars, JGRE, 130, e2024JE008724
Makkonen, L., & Tikanmäki, M. 2014, Modeling the Friction of Ice, CRST, 102, 84
Malin, M. C., Bell III, J. F., Cantor, B. A., et al. 2007, Context Camera Investigation on Board the Mars Reconnaissance Orbiter, JGRE, 112, E05S04
Malin, M. C., & Edgett, K. S. 1999, Oceans or Seas in the Martian Northern Lowlands: High Resolution Imaging Tests of Proposed Coastlines, GeoRL, 26, 3049
Mangold, N., Allemand, P., Duval, P., Geraud, Y., & Thomas, P. 2002, Experimental and Theoretical Deformation of Ice–Rock Mixtures: Implications on Rheology and Ice Content of Martian Permafrost, P&SS, 50, 385
McEwen, A. S., Delamere, W. A., Eliason, E. M., et al. 2002, Hirise: The High Resolution Imaging Science Experiment for Mars Reconnaissance Orbiter, LPSC, 33, 1163
McEwen, A. S., Eliason, E. M., Bergstrom, J. W., et al. 2007, Mars Reconnaissance Orbiter's High Resolution Imaging Science Experiment (HiRISE), JGRE, 112, E05S02
Michael, G. G., & Neukum, G. 2010, Planetary Surface Dating from Crater Size–Frequency Distribution Measurements: Partial Resurfacing Events and Statistical Age Uncertainty, E&PSL, 294, 223
Mouginis-Mark, P. J., & Boyce, J. M. 2012, Tooting Crater: Geology and Geomorphology of the Archetype Large, Fresh, Impact Crater on Mars, Geoch, 72, 1
Murray, J. B., Muller, J. P., Neukum, G., et al. 2005, Evidence from the Mars Express High Resolution Stereo Camera for a Frozen Sea Close to Mars' Equator, Natur, 434, 352
Neukum, G., Ivanov, B. A., & Hartmann, W. K. 2001, Cratering Records in the Inner Solar System in Relation to the Lunar Reference System, SSRv, 96, 55
Neukum, G., & Jaumann, R. 2004, HRSC: The High Resolution Stereo Camera of Mars Express, in ESA SP-1240, Mars Express: the Scientific Payload, ed. A. Wilson (ESA Publications Division), 17
Page, D. P. 2010, Resolving the Elysium Controversy: An Open Invitation to Explain the Evidence, P&SS, 58, 1406
Parker, T. J. 1994, Martian Paleolakes and Oceans, PhD thesis, Univ. So. California
Parker, T. J., Grant, J. A., & Franklin, B. J. 2010, The Northern Plain: A Martian Oceanic Basin?, in Lakes on Mars, ed. N. A. Cabrol & E. A. Grin (Elsevier), 249
Parmerter, R. R., & Coon, M. D. 1972, Model of Pressure Ridge Formation in Sea Ice, JGR, 77, 6565
Pathare, A. V., Paige, D. A., & Turtle, E. 2005, Viscous Relaxation of Craters within the Martian South Polar Layered Deposits, Icar, 174, 396
Peck, D. L., Wright, T. L., & Decker, R. W. 1979, The Lava Lakes of Kilauea, SciAm, 241, 114
Petrovic, J. J. 2003, Review Mechanical Properties of Ice and Snow, JMatS, 38, 1
Plescia, J. B. 1990, Recent Flood Lavas in the Elysium Region of Mars, Icar, 88, 465
Plescia, J. B. 2003, Cerberus Fossae, Elysium, Mars: A Source for Lava and Water, Icar, 164, 79
Rice, J. W., Jr, Parker, T. J., Russell, A. J., & Knudsen, O. 2002, Morphology of Fresh Outflow Channel Deposits on Mars, LPSC, 33, 2026
Richter-Menge, J. R., & Jones, K. F. 1993, The Tensile Strength of First-Year Sea Ice, JGlac, 39, 609
Rodriguez, J. A., Fairen, A. G., Tanaka, K. L., et al. 2016, Tsunami Waves Extensively Resurfaced the Shorelines of an Early Martian Ocean, NatSR, 6, 25106
Ryan, A. J., & Christensen, P. R. 2012, Coils and Polygonal Crust in the Athabasca Valles Region, Mars, as Evidence for a Volcanic History, Sci, 336, 449
Schulson, E. M., & Duval, P. 2009, Creep and Fracture of Ice (Cambridge Univ. Press)
Smith, D. E., Zuber, M. T., Frey, H. V., Sun, X., et al. 2001, Mars Orbiter Laser Altimeter: Experiment Summary after the First Year of Global Mapping of Mars, JGR, 106, 23689
Tanaka, K. L., Robbins, S. J., Fortezzo, C. M., Skinner, J. A., Jr, & Hare, T. M. 2014, The Digital Global Geologic Map of Mars: Chronostratigraphic Ages, Topographic and Crater Morphologic Characteristics, and Updated Resurfacing History, P&SS, 95, 11
Thomas, P., Squyres, S., Herkenhoff, K., Howard, A., & Murray, B. 1992, Polar Deposits of Mars, in Mars, ed. H. H. Kieffer et al. (Univ. Arizona Press), 767

Thomson, B. J., & Head, J. W. 2001, Utopia Basin, Mars: Characterization of Topography and Morphology and Assessment of the Origin and Evolution of Basin Internal Structure, JGR, 106, 23209

Timco, G. W., & Weeks, W. F. 2010, A Review of the Engineering Properties of Sea Ice, CRST, 60, 107

Voigt, J. R., & Hamilton, C. W. 2018, Investigating the Volcanic Versus Aqueous Origin of the Surficial Deposits in Eastern Elysium Planitia Mars, Icar, 309, 389

Wadhams, P. 2000, Ice in the Ocean (Gordon and Breach Science Publishers)

Watters, T. R., Campbell, B. A., Leuschen, C. J., et al. 2024, Evidence of Ice-Rich Layered Deposits in the Medusae Fossae Formation of Mars, GeoRL, 51, e2023GL105490

Watters, W. A., Geiger, L. M., Fendrock, M., & Gibson, R. 2015, Morphometry of Small Recent Impact Craters on Mars: Size and Terrain Dependence, Short-Term Modification, JGRE, 120, 226

Williams, R. M., & Malin, M. C. 2004, Evidence for Late Stage Fluvial Activity in Kasei Valles, Mars, JGRE, 109, E06001

Zegers, T. E., Oosthoek, J. H., Rossi, A. P., Blom, J. K., & Schumacher, S. 2010, Melt and Collapse of Buried Water Ice: An Alternative Hypothesis for the Formation of Chaotic Terrains on Mars, E&PSL, 297, 496